Implicit Virtual Leader: Decentralized Vision-Only Relative Pose Estimation for Multi-Robot Formations

Shiyuan Yang*, Zelin Wang*, Zhijia Tao, Yilin Wang,
Zhengyu Hou, Xiaosong Kong, Borong Zhang, Yip Fun Yeung,
Yuankai Luo, Sharon Lee, Qingbiao Li

arXiv:2607.15708v1 [cs.RO] 17 Jul 2026

***Abstract*— Classical leader-follower formation control suffers from single points of failure and error propagation, and relies on absolute localization sensors that are ill-suited for GPS-denied environments. We address these limitations by introducing a fully decentralized, vision-only relative pose estimation framework based on Graph Neural Networks (GNNs). The key idea is the implicit virtual leader (IVL): a non-physical formation reference frame that is not tied to any individual robot but is implicitly learned within the GNN using only monocular images and inter-robot communication. We attach a heteroscedastic GNLL head for aleatoric uncertainty and MC Dropout for epistemic uncertainty, and conduct a systematic comparison across simulation and real-world test sets. Our framework achieves competitive pose estimation accuracy and generalizes naturally to heterogeneous robot platforms and varying formation sizes.**

I. Introduction

Multi-robot systems (MRS) are increasingly used to tackle complex tasks that are beyond the capabilities of a single robot, including exploration [1], search and rescue [2], environmental monitoring [3], and cargo delivery [4]–[6]. In MRS, formation control is a general capability for enabling cooperative tasks; it requires coordinating multiple robots to maintain a desired geometric configuration [7]. Existing strategies include leader-follower, virtual structure, and behavior-based approaches [8].

The leader-follower approach is popular for its simplicity, but the dependence on a designated leader introduces a single point of failure and error propagation [9], [10]. Furthermore, most formation control methods assume that each robot's absolute pose is available through GPS, LiDAR, or other dedicated sensors. These sensors can be power-hungry, bulky, and unreliable in GPS-denied or indoor environments. Monocular cameras offer a low cost alternative, but using them for pose estimation in formation control remains challenging due to sensitivity to lighting, lack of depth information, and the need for robust feature matching.

To address these challenges, we propose a decentralized relative pose estimation architecture driven solely by vision and Graph Neural Networks (GNNs). Our key idea is the implicit virtual leader (IVL): a non-physical formation reference frame that is not tied to any individual robot. Instead, it is implicitly learned within the GNN via inter-robot communication and monocular images. This eliminates both the single-point-of-failure vulnerabilities of leader-follower mechanisms and the reliance on external localization sensors typical of classical virtual leader approaches. We validate our method on a heterogeneous robot team comprising wheeled and quadruped platforms. The primary contributions are:

1) We introduce IVL, a formation reference frame implicitly learned within a GNN. This enables decentralized relative pose estimation while effectively resolving single-point-of-failure.
2) We design a Transformer-based GNN that regresses each robot's pose relative to the IVL directly from monocular images. The architecture enables distributed, real-time inference directly on onboard robot hardware, removing the reliance on absolute localization sensors or prior maps.
3) We equip the IVL estimator with aleatoric uncertainty via heteroscedastic GNLL and epistemic uncertainty via MC Dropout; experiments show that aleatoric uncertainty dominates across both simulation and real-world test sets.
4) We show that one trained model deploys on heterogeneous formations without fine-tuning, validating its precision in real-world experiments.

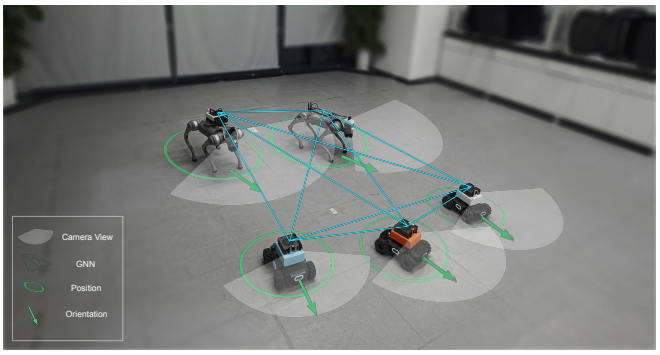


Fig. 1. Conceptual illustration of the proposed approach. Each robot uses only a monocular camera and inter-robot communication to estimate its relative pose with respect to an implicit virtual leader (IVL).

II. Related Work

Multi-robot formation control. Leader-follower and virtual structure paradigms have historically dominated multi-robot formation control [11]–[17], but both remain vulnerable in GPS-denied or cluttered environments. Leader-follower methods introduce single points of failure through leader

*These authors contributed equally.

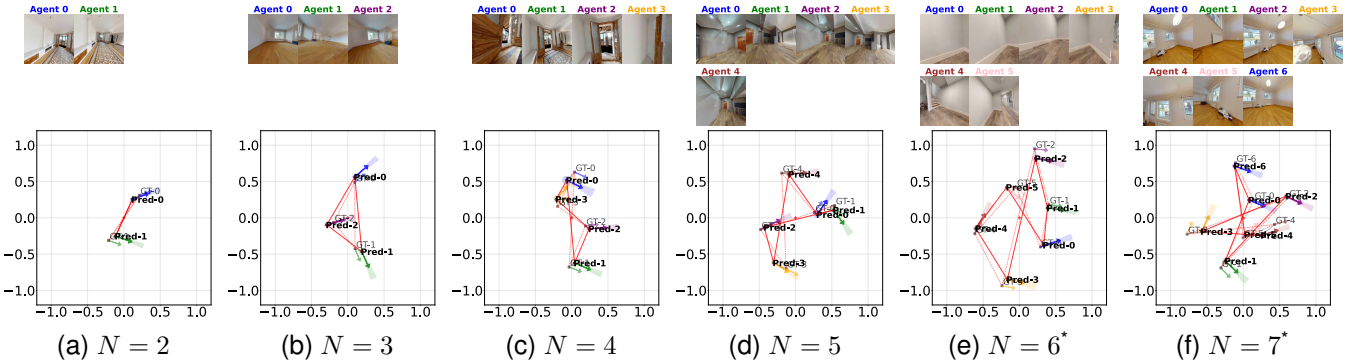


Fig. 2. Qualitative pose with uncertainty visualization for team sizes $N \in \{2, 3, 4, 5, 6, 7\}$. Solid markers indicate predicted poses; dashed markers indicate ground truth. Red lines connect each prediction to its ground truth position. The cross at the origin denotes the IVL. Uncertainty is visualized as position variance circles and orientation fan sectors. Asterisked sizes ($N \geq 6$) are unseen during training.

dependence, while virtual structures often require global pose synchronization and centralized computation, limiting robustness under sensing, communication, and obstacle-induced disturbances.

Virtual leaders. Researchers have proposed non-physical virtual leaders (VL) to guide robot teams [17]–[19], mitigating the single-point-of-failure inherent to leader-follower structures. Our implicit virtual leader (IVL) extends this idea along three axes: (i) the reference frame is a statistical aggregate of the team's poses inferred from data, rather than a designer-prescribed trajectory; (ii) it is computed implicitly inside the GNN from monocular images and inter-robot embeddings, requiring no absolute pose at inference; (iii) inference is fully node-level decentralized, with no shared global state across the team.

GNNs-based pose estimation. GNNs have been widely adopted in multi-robot systems due to their natural ability to model communication topologies, facilitate decentralized computation, and ensure scalability [20], [21]. For instance, Blumenkamp et al. [22] estimate inter-robot poses relative to a designated physical leader. However, this pairwise, leader-centric formulation remains susceptible to typical leader-follower issues. Our IVL formulation instead estimates poses relative to a learned non-physical reference.

III. Problem Formulation

We consider a team of N mobile robots. Absolute poses are unavailable due to sensing or environmental constraints; each robot i observes only a monocular RGB image $\mathbf{O}_i \in \mathbb{R}^{W \times H \times 3}$. Inter-robot communication is modeled as a directed graph $\mathcal{G} = (\mathcal{V}, \mathcal{E})$, where $\mathcal{V} = \{1, \ldots, N\}$, and $\mathcal{E}$ denotes communication links. Thus, robots exchange learned feature embeddings over a communication graph within a distance threshold. We define an implicit virtual leader (IVL) $L_v = (\mathbf{p}_v, \mathbf{q}_v)$ as a non-physical reference frame associated with the formation centroid. The goal is to learn a distributed estimator f_θ that maps each robot's local observation and exchanged embeddings to its 6-DoF pose relative to the IVL, without absolute localization.

IV. Methods

A. IVL Formulation

The position of the IVL is defined as the centroid of the team:

$$\mathbf{p}_v = \frac{1}{N} \sum_{i=1}^{N} \mathbf{p}_i. \tag{1}$$

The orientation $\mathbf{q}_v$ is computed as the principal eigenvector of the quaternion correlation matrix:

$$\mathbf{M} = \sum_{i=1}^{N} \mathbf{q}_i \mathbf{q}_i^\top, \quad \mathbf{q}_v = \arg\max_{\|\mathbf{q}\|=1} \mathbf{q}^\top \mathbf{M} \mathbf{q}, \tag{2}$$

A small constant weight perturbation is applied to the first robot to break degeneracy and guarantee a unique principal eigenvector.

$$\mathbf{q}_i^{\text{rel}} = \mathbf{q}_v^{-1} \otimes \mathbf{q}_i, \tag{3}$$

$$\mathbf{p}_i^{\text{rel}} = \mathbf{R}(\mathbf{q}_i)^\top (\mathbf{p}_i - \mathbf{p}_v), \tag{4}$$

where $\mathbf{R}(\cdot)$ denotes the rotation matrix corresponding to a given quaternion and $\otimes$ denotes quaternion multiplication; we abbreviate $\mathbf{R}_i \triangleq \mathbf{R}(\mathbf{q}_i)$ and $\mathbf{R}_v \triangleq \mathbf{R}(\mathbf{q}_v)$ where convenient.

The relative orientation $\mathbf{q}_i^{\text{rel}}$ is expressed in the IVL frame while the relative position $\mathbf{p}_i^{\text{rel}}$ is expressed in robot i's body frame. This asymmetry is deliberate: orientation differences are frame invariant, so $\mathbf{q}_i^{\text{rel}}$ is well defined once $\mathbf{q}_v$ is aggregated. Position offsets, in contrast, are directional vectors whose components depend on the reference frame. Expressing the position target in the IVL frame would couple the prediction frame ($\mathbf{R}_v$) with the input visual frame ($\mathbf{R}_i$) in a sample dependent way, breaking input-output equivariance and, in our experiments, causing training to stagnate. The body frame formulation in Eq. (4) avoids this by mapping the centroid offset into a fixed geometry regardless of each robot's global orientation, as illustrated in Fig. 3.

In addition to pose estimates, the model outputs associated aleatoric uncertainty: a positional variance $\hat{\boldsymbol{\sigma}}_{p,i}^2 \in \mathbb{R}^3$ and an

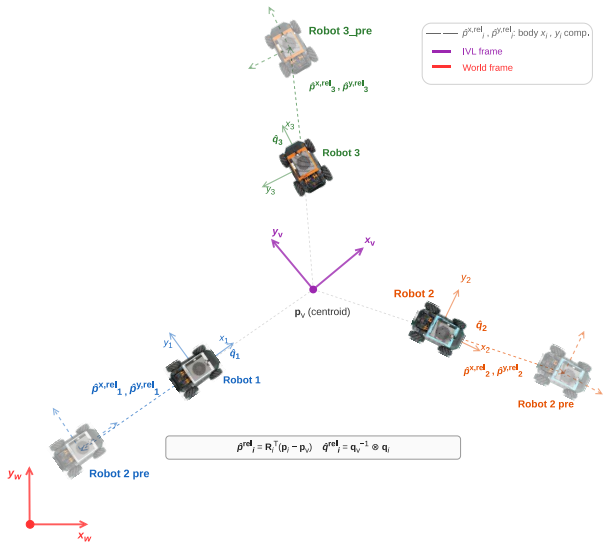


Fig. 3. Body frame relative position formulation. By expressing the relative position in its own egocentric frame, the mapping from visual features to spatial offsets remains geometrically consistent regardless of the robot's global orientation.

orientation variance $\hat{\sigma}^2_{q,i} \in \mathbb{R}$. The complete per robot output is an 11 dimensional vector:

$$\hat{\mathbf{y}}_i = [\hat{\mathbf{p}}_i^{\text{rel}},\ \hat{\boldsymbol{\sigma}}^2_{p,i},\ \hat{\mathbf{q}}_i^{\text{rel}},\ \hat{\sigma}^2_{q,i}] \in \mathbb{R}^{11}. \tag{5}$$

B. Overall Architecture

Our method applies a GNN over the communication graph $\mathcal{G}$ defined in Section III. Each robot encodes its local observation, exchanges embeddings with neighbors, and decodes the aggregated node representation into its pose relative to the IVL. Mathematically, for robot i, the pipeline operates as follows:

$$\mathbf{z}_i = f_{\text{enc}}(\mathbf{O}_i), \tag{6}$$

$$\mathbf{h}_i = f_{\text{gnn}}\left(\mathbf{z}_i, \{\mathbf{z}_j \mid j \in \mathcal{N}_i\}\right), \tag{7}$$

$$\hat{\mathbf{y}}_i = f_{\text{dec}}(\mathbf{h}_i), \quad i = 1, 2, \ldots, N. \tag{8}$$

Here, f_{enc} encodes each robot's local observation $\mathbf{O}_i$ into a feature embedding $\mathbf{z}_i \in \mathbb{R}^{L\times C}$. The GNN module f_{gnn} jointly processes robot i's own features and those received from its neighbors $j \in \mathcal{N}_i$ via edge-level message passing, producing a compact node representation $\mathbf{h}_i$. Finally, f_{dec} decodes $\mathbf{h}_i$ into the estimated relative pose $\hat{\mathbf{y}}_i \in \mathbb{R}^{11}$ as defined in Eq. (5). The proposed architecture is shown in Fig. 4.

Encoder. The image encoder f_{enc} maps each robot's observation to a compact feature sequence. We use a frozen DINOv2 ViT-S/14 [23] backbone followed by a multi-layer Transformer [24] module that progressively reduces both the feature dimension and the sequence length. Each layer applies self-attention with residual connections, a feature-axis linear projection that progressively reduces the channel dimension, a sequence-truncation step, and a layer normalization, yielding

$$\mathbf{z}_i = f_{\text{enc}}(\mathbf{O}_i) \in \mathbb{R}^{L\times C}, \qquad L = C = 64, \tag{9}$$

where f_{enc} compresses the DINOv2 token tensor by an order of magnitude while preserving per-token spatial structure for downstream message passing.

GNN. The GNN module f_{gnn} refines per-robot feature sequences $\{\mathbf{z}_i\}$ through two stage Transformer message passing on $\mathcal{G}$. First, each directed edge $(j \to i)$ processes the paired endpoint sequences to produce an edge message $\mathbf{m}_{ij} \in \mathbb{R}^{64}$, which is aggregated into an initial node embedding $\mathbf{x}_i^{(0)}$. Second, vector level edge features are jointly refined and aggregated back to each node, yielding the final representation $\mathbf{h}_i$.

Decoder. The decoder regresses an 11-dimensional output for each robot:

$$\hat{\mathbf{y}}_i = [\hat{\mathbf{p}}_i, \hat{\boldsymbol{\sigma}}^2_{p,i}, \hat{\mathbf{q}}_i, \hat{\sigma}^2_{q,i}], \tag{10}$$

where $\hat{\mathbf{p}}_i \in \mathbb{R}^3$ and $\hat{\mathbf{q}}_i \in \mathbb{R}^4$ are the predicted relative position and L2-normalized orientation, and $\hat{\boldsymbol{\sigma}}^2_{p,i} \in \mathbb{R}^3$, $\hat{\sigma}^2_{q,i} \in \mathbb{R}$ are their associated variances.

C. Uncertainty Estimation

We model both aleatoric and epistemic uncertainty [25]. The aleatoric component is captured by the variance heads in Eq. (5) and trained jointly with the regression loss; the epistemic component is obtained at inference time via MC Dropout.

1) Aleatoric Uncertainty via Heteroscedastic GNLL: For position, we follow the heteroscedastic regression formulation of [26] and minimize a Gaussian negative log-likelihood (GNLL) with a diagonal covariance:

$$\mathcal{L}_{\text{pos}} = \tfrac{1}{2}\sum_k \left(\log \hat{\sigma}^2_{p,i,k} + \frac{(\hat{p}_{i,k} - p^{\text{gt}}_{i,k})^2}{\hat{\sigma}^2_{p,i,k}} \right), \tag{11}$$

where k indexes the three position axes. The $\log \hat{\sigma}^2_{p,i,k}$ terms prevent the trivial solution of inflating the variances to drive the loss toward zero. For orientation, we adopt the chordal-GNLL loss [22], [27], which resolves the sign ambiguity $\mathbf{q} \equiv -\mathbf{q}$ via:

$$d_{\text{quat}} = \min(\|\hat{\mathbf{q}}_i - \mathbf{q}_i^{\text{gt}}\|_2,\ \|\hat{\mathbf{q}}_i + \mathbf{q}_i^{\text{gt}}\|_2), \tag{12}$$

$$\mathcal{L}_{\text{ori}} = \tfrac{1}{2}\left(\log \hat{\sigma}^2_{q,i} + \frac{2 d^2_{\text{quat}}(4 - d^2_{\text{quat}})}{\hat{\sigma}^2_{q,i}} \right). \tag{13}$$

At test time, the predicted variances $\hat{\boldsymbol{\sigma}}^2_{p,i}$ and $\hat{\sigma}^2_{q,i}$ are interpreted as the aleatoric uncertainty of the corresponding pose component.

2) Epistemic Uncertainty via MC Dropout: To capture model uncertainty, we keep dropout layers in the GNN and the pose decoder active at inference time and perform $T = 30$ stochastic forward passes per input [28]. The DINOv2 backbone is deterministic and frozen; we cache its features once per image so each MC pass only re-evaluates the GNN and decoder, which keeps inference cost modest.

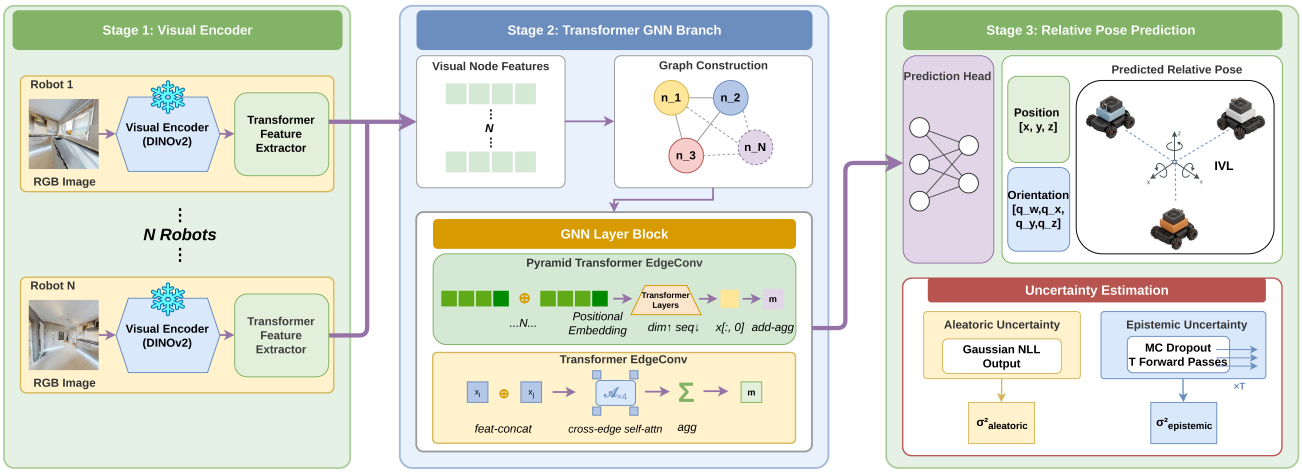


Fig. 4. Overview of the IVL framework architecture. Each robot encodes its monocular image via a frozen DINOv2 backbone. A two stage Transformer based GNN aggregates inter-robot embeddings over the communication graph. The decoder produces each robot's 6-DoF pose relative to the IVL together with its heteroscedastic aleatoric uncertainty, while epistemic uncertainty is obtained at inference time via MC Dropout.

The epistemic variance ($\boldsymbol{\sigma}^2_{\text{epi},i}$) is the sample variance over the T predictions:

$$\boldsymbol{\sigma}^2_{\text{epi},i} = \frac{1}{T}\sum_{t=1}^{T}\big(\hat{\mathbf{y}}_i^{(t)} - \bar{\mathbf{y}}_i\big)^2, \quad \bar{\mathbf{y}}_i = \tfrac{1}{T}\textstyle\sum_t \hat{\mathbf{y}}_i^{(t)}. \tag{14}$$

We treat aleatoric and epistemic uncertainty as separate, complementary signals rather than combining them into a single scalar, as compared in Section V-C.

D. Training Objective

We train the network under an imitation learning paradigm: at each training step, ground truth 6-DoF poses $(\mathbf{p}_i^{\text{rel}}, \mathbf{q}_i^{\text{rel}})$ obtained from a simulator or mocap system serve as expert demonstrations, and the network learns to imitate this expert by minimising the discrepancy between its predictions and the demonstrated poses. The total objective combines three complementary terms:

$$\mathcal{L}_{\text{total}} = \mathcal{L}_{\text{pos}} + \mathcal{L}_{\text{ori}} + \mathcal{L}_{\text{relpos}}, \tag{15}$$

where $\mathcal{L}_{\text{pos}}$ and $\mathcal{L}_{\text{ori}}$ are the heteroscedastic positional GNLL and chordal orientation GNLL losses defined in Section IV-C.

To preserve formation structure, $\mathcal{L}_{\text{relpos}}$ penalizes pairwise relative position errors in a common frame. Optimizing $\mathcal{L}_{\text{pos}}$ and $\mathcal{L}_{\text{ori}}$ independently treats each robot as a separate regression target, which can yield locally plausible poses but distort the global formation geometry. The relative position loss provides a structural constraint by matching pairwise offsets across the formation.

We lift body frame predictions to a common frame using the corresponding relative orientations:

$$\mathbf{w}_i^{\text{pred}} = \mathbf{R}(\hat{\mathbf{q}}_i^{\text{rel}})\,\hat{\mathbf{p}}_i^{\text{rel}}, \tag{16}$$

$$\mathbf{w}_i^{\text{gt}} = \mathbf{R}(\mathbf{q}_i^{\text{rel}})\,\mathbf{p}_i^{\text{rel}}, \tag{17}$$

and define

$$\mathcal{L}_{\text{relpos}} = \frac{2}{N(N-1)}\sum_{i<j}\Big\|(\mathbf{w}_i^{\text{pred}} - \mathbf{w}_j^{\text{pred}}) - (\mathbf{w}_i^{\text{gt}} - \mathbf{w}_j^{\text{gt}})\Big\|_1. \tag{18}$$

This structural term discourages collapse by requiring the predicted formation to preserve the pairwise geometry.

E. Training Details

Excluding the frozen DINOv2 backbone, our model contains approximately 8.4 M trainable parameters. We use the HM3D dataset, partitioned into 638 training, 152 validation, and 8 test scenes, yielding a total of 800 k formation samples. Each sample contains a varying number of robots, with the team size N randomly drawn from $\{2, \ldots, 5\}$. To assemble a formation, rendered viewpoints within a scene are grouped into navigable-point clusters; each sample takes N distinct clusters on the same floor with one image per cluster, and all pairwise distances stay within the 2.0 m formation diameter. Input images are resized to 224×224 pixels. Training runs for 15 epochs with a batch size of 64 on a single NVIDIA RTX 5090 GPU using bf16 mixed precision, requiring approximately 9 hours to converge.

V. Experimental Results

We evaluate the proposed method to answer the following key questions:

- **Q1:** Does the IVL-based formulation accurately estimate relative poses across varying formation sizes, and does the relative position loss effectively prevent formation collapse?
- **Q2:** Do the predicted uncertainty estimates faithfully reflect actual errors and remain reliable under sim-to-real domain shift?
- **Q3:** Does the model generalize to entirely unseen environments without fine-tuning?
- **Q4:** Can the system be deployed on heterogeneous robot platforms and operate in real-world formation control?

TABLE I

POSE ESTIMATION ACCURACY ON THE HM3D TEST SPLIT (8 SCENES, $N \in \{2,3,4,5\}$, 989,962 SAMPLES, POOLED MEDIAN); SAMPLES ARE OBTAINED BY ENUMERATING ALL N-SUBSETS AT EACH TEST TIMESTAMP. POSITION IN METERS, ORIENTATION IN DEGREES. VISIBILITY: $|\Delta\psi| < 120°$; FILTERING USES YOUDEN'S INDEX ON PREDICTED VARIANCE $\hat{\sigma}_p$. BEST PER COLUMN IN **BOLD**.

Method	All		Visible		Invisible		Invis. Filt.	
	pos	ori	pos	ori	pos	ori	pos	ori
CoViS-Net [22]	0.403	8.3	0.279	7.5	0.442	8.5	**0.222**	6.8
Ours	**0.277**	**6.7**	**0.199**	**4.6**	**0.305**	**8.4**	0.230	**5.8**

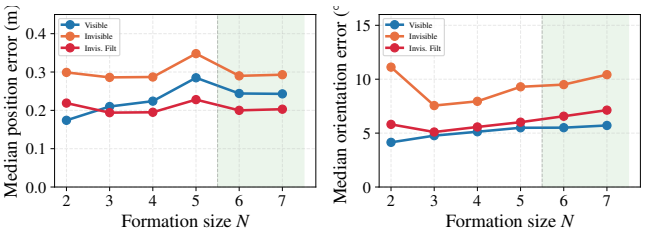


Fig. 5. Median pose errors across formation sizes $N \in \{2,\ldots,7\}$ for four conditions: Visible, Visible+Filtered (Vis. Filt), Invisible, and Invisible+Filtered (Invis. Filt). The green shaded region marks formation sizes unseen during training ($N > 5$).

A. Experimental Setup

1) HM3D (Habitat Matterport3D) Dataset: We evaluate on the 8 HM3D [29] test scenes described in Section IV-E, which are entirely unseen during training. Each scene provides photorealistic multi-room indoor renderings with ground truth 6-DoF camera poses used as the evaluation reference.

2) CoViS-Net Test Set: We use the CoViS-Net real-world benchmark [22], which spans diverse indoor environments and one outdoor scene with LiDAR-based ground truth, as an out-of-distribution (OOD) test set. To assess sim-to-real generalization, the model trained in simulation is directly evaluated on the real-world dataset without any fine-tuning.

3) Real-world Platform: Our real-world experimental platform comprises three modified DJI RoboMaster (RM) wheeled robots and one Unitree Go2 quadruped. Each RM is equipped with a monocular RGB camera (148° field of view) and an NVIDIA Jetson AGX Orin compute module. Similarly, the quadruped is retrofitted with the identical camera model, alongside a Jetson Orin Nano. Experiments are conducted in a 6.3×5.1 m indoor laboratory arena, where ground truth 6-DoF poses are recorded using a mocap system.

B. Pose Estimation Accuracy

To answer Q1, we evaluate position and orientation accuracy across varying formation sizes. Since both predictions and ground truth labels are expressed as relative poses (Section IV-A), errors are computed in this relative coordinate system. The position error for robot i is the Euclidean distance between the predicted and ground truth body frame offsets:

$$e_p^i = \|\hat{\mathbf{p}}_i^{\mathrm{rel}} - \mathbf{p}_i^{\mathrm{rel,gt}}\|_2, \tag{19}$$

where $\mathbf{p}_i^{\mathrm{rel}} = \mathbf{R}_i^\top(\mathbf{p}_i - \mathbf{p}_v)$ denotes the centroid offset rotated into robot i's body frame. The orientation error is the geodesic distance between the predicted and ground truth relative quaternions:

$$e_q^i = 2\arccos(|\langle \hat{\mathbf{q}}_i^{\mathrm{rel}}, \mathbf{q}_i^{\mathrm{rel,gt}} \rangle|), \tag{20}$$

where $\mathbf{q}_i^{\mathrm{rel}} = \mathbf{q}_v^{-1} \otimes \mathbf{q}_i$, expressed in degrees. We report median errors to reduce sensitivity to outliers.

We benchmark our model against CoViS-Net [22] on 8 indoor test scenes split from the HM3D dataset in Table I. Both methods are trained on HM3D and evaluated on the same eight unseen scenes. We report the pooled median error over all formation sizes $N \in \{2,3,4,5\}$ across 989,962 samples. A pair of nodes is classified as visible if the two cameras share FOV overlap ($|\Delta\psi| < 120°$) and invisible otherwise. High uncertainty predictions are further rejected by Youden's index on the predicted variance $\hat{\sigma}_p$. As shown in Table I, our IVL-based formulation achieves accuracy highly competitive with the state-of-the-art CoViS-Net baseline across both visible and invisible conditions.

We further evaluate performance per formation size on HM3D across $N \in \{2,\ldots,7\}$; the model is trained on $N \in \{2,\ldots,5\}$, so $N \in \{6,7\}$ are entirely unseen. Fig. 5 breaks down errors by visibility and uncertainty filtering; the trends mirror Table I. Performance remains stable on the unseen sizes: position error is 0.29 m for both $N = 6$ and $N = 7$, with orientation errors of 9.3° and 10.3° respectively. This demonstrates that the GNN based architecture naturally generalizes to larger teams, as each node's prediction depends only on aggregated neighbor features rather than a fixed team size.

C. Uncertainty Estimation Evaluations

To answer Q2, we use three complementary metrics to evaluate uncertainty quality [30], [31]:

1) **ECE** [30] (Expected Calibration Error) measures calibration fidelity by binning predictions and comparing mean variance estimate $\bar{\sigma}_b$ to mean absolute error $\bar{e}_b$ in each bin b:

$$\mathrm{ECE} = \sum_b \frac{|B_b|}{n} |\bar{\sigma}_b - \bar{e}_b|, \tag{21}$$

where $|B_b|$ is the bin count and n is the total number of samples. A lower ECE indicates a smaller gap between predicted confidence and actual error magnitudes, and therefore greater reliability.

2) **AUSE** [31] (Area Under the Sparsification Error curve) measures filtering utility: samples are progressively removed in order of decreasing uncertainty and prediction error is recomputed at each removal fraction θ:

$$\mathrm{AUSE} = \int_0^1 \left[E(\theta) - E_{\mathrm{oracle}}(\theta)\right] d\theta, \tag{22}$$

where $E(\theta)$ is the error after removing fraction θ by uncertainty and $E_{\mathrm{oracle}}(\theta)$ removes by true error. The lower

TABLE II

UNCERTAINTY SOURCE COMPARISON ON THE SIMULATION ($D_{\text{TEST}}^{\text{SIM}}$) AND REAL-WORLD ($D_{\text{TEST}}^{\text{REAL}}$) TEST SETS. BEST PER COLUMN IN **BOLD**. ECE: EXPECTED CALIBRATION ERROR; AUSE: AREA UNDER SPARSIFICATION ERROR CURVE; ρ: SPEARMAN RANK CORRELATION BETWEEN UNCERTAINTY AND ERROR.

Setting	Source	Position			Orientation		
		ECE↓	AUSE↓	ρ↑	ECE↓	AUSE↓	ρ↑
Simulation	Aleatoric	**0.022**	**0.169**	**0.676**	**0.113**	**0.174**	**0.663**
	Epistemic	0.241	0.419	0.223	0.425	0.265	0.600
Real-world	Aleatoric	**0.037**	**0.235**	**0.473**	**0.082**	**0.176**	**0.386**
	Epistemic	0.173	0.302	0.360	0.339	0.244	0.374

the AUSE, the better uncertainty identifies unreliable predictions.

3) **Spearman** ρ measures the monotonic rank correlation between predicted uncertainty and actual error:

$$\rho = 1 - \frac{6\sum_{i=1}^{n} d_i^2}{n(n^2-1)}, \tag{23}$$

where d_i is the difference between the rank of the predicted uncertainty $\hat{\sigma}_i$ and the rank of the actual error e_i, and n is the total number of samples. The higher the ρ, the more reliable the uncertainty signal is as a ranking proxy, even when absolute magnitudes are miscalibrated.

We compare aleatoric and epistemic uncertainty on both the simulation test set (HM3D $D_{\text{Test}}^{\text{Sim}}$) and the real-world test set (CoViS-Net $D_{\text{Test}}^{\text{Real}}$). Table II reports the three metrics for position and orientation, and Fig. 6 shows the corresponding sparsification curves.

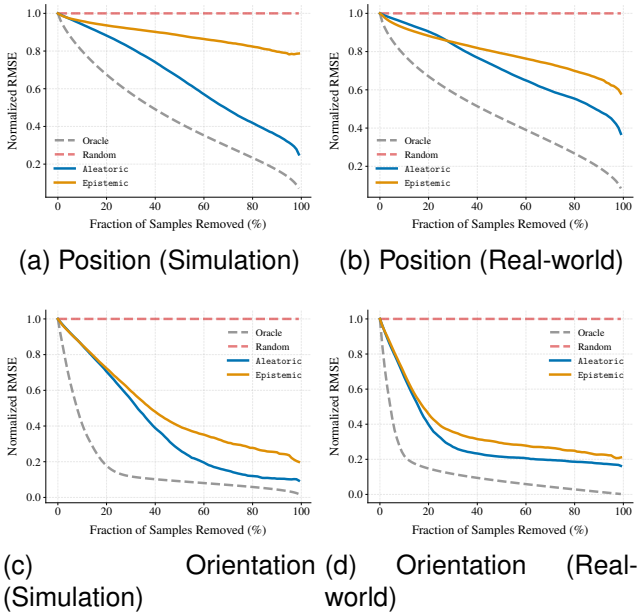


Fig. 6. Sparsification curves for aleatoric and epistemic uncertainty. Samples are removed by decreasing uncertainty; oracle (grey dashed line) removal by true error gives the lower bound curve, while random removal (red dotted line) is the uninformative baseline. Both uncertainty sources outperform random removal across all panels.

The consistent pattern across both regimes appears to reflect a structural difference between the two uncertainty sources. We hypothesize that, because the heteroscedastic GNLL head learns a sample conditioned variance tied to the regression loss, the same gradient that fits the mean may also push ambiguous samples (low FOV overlap, repetitive geometry, motion blur) toward larger predicted variance $\hat{\sigma}^2$. MC Dropout, by contrast, samples function space perturbations from a data independent mask distribution, so its variance plausibly tracks parameter sensitivity at the input rather than the actual prediction error. Epistemic curves still sit clearly above the random baseline in Fig. 6, so MC Dropout does carry useful information about prediction reliability. However, parameter-sensitivity rankings are only weakly aligned with the visual cues that drive error, whereas aleatoric uncertainty preserves a stronger ordering, as shown in Table II, and is more robust to domain shift.

TABLE III

CROSS-DATASET GENERALIZATION ON COVIS-NET $D_{\text{TEST}}^{\text{REAL}}$ SCENES WITHOUT FINE-TUNING ($N \in \{2,3,4,5\}$). POSITION IN METERS, ORIENTATION IN DEGREES. VISIBILITY: $|\Delta\psi| < 120°$; FILTERING USES YOUDEN'S INDEX ON PREDICTED UNCERTAINTY $\hat{\sigma}_p$. BEST PER COLUMN IN **BOLD**.

Method	All		Visible		Invisible		Invis. Filt.	
	pos	ori	pos	ori	pos	ori	pos	ori
CoViS-Net [22]	0.632	7.934	0.396	6.219	0.730	**8.624**	**0.297**	**5.705**
Ours	**0.438**	**7.746**	**0.298**	**4.069**	**0.500**	11.204	0.391	6.842

D. Cross-Scene Generalization

To answer Q3, we evaluate cross-scene generalization by testing our HM3D trained model on the CoViS-Net real-world dataset [22] without fine-tuning. Each sample is an N-tuple of synchronized monocular frames; we extend the original N=3 triplet protocol to $N \in \{2,3,4,5\}$ by enumerating all N-subsets of robots at each timestamp, yielding 56,032 samples. Both methods are evaluated on the same sample list and the same input frames, with each backbone's expected preprocessing, and pooled median errors are reported at each method's native granularity. High uncertainty predictions on the invisible subset are further rejected using Youden's index on $\hat{\sigma}_p$.

Table III reports cross-scene generalization. For a fair comparison, CoViS-Net results are obtained by evaluating the authors' publicly released model weights on the same samples under identical metrics. Our model outperforms CoViS-Net on position across all three unfiltered regimes (pooled position error: 0.438 m vs. 0.632 m, a 31% reduction) and on orientation in the visible setting, while CoViS-Net retains a slight edge on invisible orientation. After uncertainty filtering on the invisible subset, both models show obvious improved performance. Overall, both models trained purely on HM3D transfer to unseen real-world scenes, and the IVL formulation is competitive with the CoViS-Net pairwise baseline at $N \in \{2,3,4,5\}$.

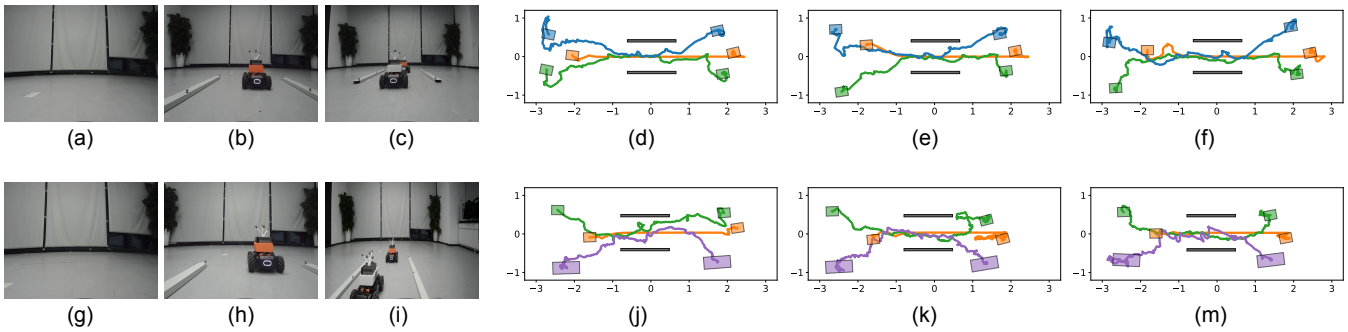


Fig. 7. **Homogeneous 3 RM and heterogeneous 2 RM+1 quadruped** setups. Left panels show in tunnel camera views. Right panels show top-down mocap trajectories traversing the tunnel. Colored lines are the mocap recorded paths of the mocap driven robot (RM_0, orange) and our network driven robots (RM_1, green; RM_2, blue; quadruped, purple). Gray rectangles mark the two parallel walls.

E. Tunnel Traversal Experiment

To answer Q4, we conduct two complementary sets of multi-robot formation morphing tunnel traversal experiments in a laboratory environment. In both setups, three robots approach a narrow tunnel in triangular formation, transition to a column formation at the entrance, traverse the corridor, and recover to triangular formation on exit. The first setup uses a homogeneous team of three RM wheeled robots (RM_0, RM_1, RM_2); the second replaces RM_2 with a Unitree Go2 quadruped, yielding a heterogeneous team with wheeled and quadruped robots that additionally stresses the model under platform diversity. The GNN model deployed here is trained entirely on real-world data. We collect this data by letting a single RM robot autonomously perform a random walk through our laboratory arena in an empty configuration, recording its onboard camera images together with the corresponding ground truth poses from the mocap system.

1) Setting: We use a hybrid control architecture in which RM_0 is trajectory driven in the tunnel, uses mocap to obtain its pose, and follows a preplanned centerline via a P controller, while the remaining two robots are GNN driven and rely solely on the GNN predictions for formation control. The tunnel length is $L = 1.27\,\text{m}$ and the corridor width is $W = 0.72\,\text{m}$, which is approximately the combined width of three Robomasters. We report 12 trials for both homogeneous and heterogeneous setups.

2) Results: Fig. 7 shows mocap recorded trajectories for both setups. The team enters in triangular formation, contracts into the commanded column inside the tunnel, and reopens to triangular on exit; RM_0 with position feedback from mocap tracks its commanded centerline within $\sim$0.01 m of lateral error throughout. All 24 trials successfully complete the traversal, with 21 of 24 collision-free: the homogeneous 3 RM team is collision-free in all 12 trials, while the heterogeneous wheeled+quadruped team is collision-free in 9 of 12 trials, with the remaining trials exhibiting only brief brushing contact.

Table IV reports pose errors per phase for the two setups, from which three findings stand out. (i) Inside the tunnel, although the pose estimation error is around 0.2 m (0.197 / 0.215 m for the two setups), the GNN driven robots keep their lateral deviation from the corridor centerline within 0.065 / 0.103 m. Since this lateral deviation is the quantity that determines whether a robot clears the walls, and it stays well below the available wall clearance, both teams traverse the corridor without collision. (ii) The GNN driven quadruped attains 0.090 m in tunnel lateral deviation, closely matching the wheeled robot despite its wider body and gait induced oscillations, which shows that the perception pipeline generalizes across platforms without fine-tuning. (iii) Predicted positional uncertainty $\hat{\sigma}_p$ rises from $\sim$0.064 m in the open triangular phase to $\sim$0.086 m in the tunnel, tracking scene difficulty.

TABLE IV

POSE ERRORS PER PHASE FOR BOTH TUNNEL SETUPS, AGGREGATED ACROSS 12 TRIALS PER SETUP. EACH CELL REPORTS MEDIAN / 75TH PERCENTILE. "POSE" ROWS ARE EUCLIDEAN DISTANCE BETWEEN GNN PREDICTION AND GROUND TRUTH RELATIVE POSE; "LATERAL" ROWS ARE MOCAP MEASURED LATERAL DEVIATION FROM TUNNEL CENTERLINE.

Setup	Phase	e_p (m)	e_ψ (deg)	$\hat{\sigma}_p$ (m)
3 RM	triangle (pose)	0.158 / 0.215	1.4 / 2.4	0.070
	transition (pose)	0.148 / 0.196	1.1 / 1.6	0.080
	in tunnel (pose)	0.197 / 0.248	1.3 / 2.0	0.081
	in tunnel (lateral)	0.065 / 0.109	2.9 / 3.4	0.081
2 RM+Go2	triangle (pose)	0.238 / 0.331	1.5 / 2.6	0.064
	transition (pose)	0.208 / 0.262	1.4 / 2.3	0.084
	in tunnel (pose)	0.215 / 0.267	1.6 / 2.4	0.086
	in tunnel (lateral)	0.103 / 0.159	3.7 / 4.3	0.086

Our experimental configuration is challenging in both setups: during training the model has never seen the tunnel walls used here or the robots within the formation; in column formation, each rear robot's environmental view is largely occluded by the robot in front of it; and the cameras face large gray-white motorized curtains that are nearly textureless and provide few distinctive visual cues. Notably, the robots have no prior knowledge of the environment, including the location of the tunnel; collisions with the tunnel walls are avoided purely through vision driven formation morphing. Despite these difficulties, and despite consuming raw GNN output without temporal smoothing, both teams successfully traverse the 0.72 m corridor (roughly the combined width of three RMs), underscoring the strong generalization of our perception pipeline and delivering

feedback stable enough for direct closed loop control on both homogeneous and heterogeneous multi-robot teams.

VI. Conclusion

We presented a decentralized, vision only relative pose estimation framework for multi-robot formation control based on the IVL, a non-physical reference frame implicitly learned by a Transformer based GNN. Using only monocular images and inter-robot communication, the model estimates each robot's 6-DoF pose relative to the IVL while providing both aleatoric and epistemic uncertainty. Experiments show strong cardinality and scene generalization across 2–7 robots, effective aleatoric uncertainty under simulation and real-world tests, and direct transfer from HM3D to real-world benchmarks without fine-tuning. In physical tunnel traversal experiments, the same framework provides stable closed-loop feedback for both homogeneous and heterogeneous robot teams, enabling traversal of a narrow 0.72 m corridor, thereby demonstrating both high precision and practical generalizability.

Several limitations remain. The current framework performs single frame inference and does not exploit temporal consistency, which could further improve pose stability. A sim-to-real gap also remains under real-world domain shift. Finally, since this work focuses on perception and relative localization, future efforts will build on this framework toward integrated obstacle avoidance, planning, and navigation for multi-robot formations.

References

[1] C. Nieto-Granda, J. G. Rogers III, and H. I. Christensen, "Coordination strategies for multi-robot exploration and mapping," *The International Journal of Robotics Research*, vol. 33, no. 4, pp. 519–533, 2014.

[2] J. S. Jennings, G. Whelan, and W. F. Evans, "Cooperative search and rescue with a team of mobile robots," in *1997 8th International Conference on Advanced Robotics. Proceedings. ICAR'97*. IEEE, 1997, pp. 193–200.

[3] G. Notomista, C. Pacchierotti, and P. R. Giordano, "Multi-robot persistent environmental monitoring based on constraint-driven execution of learned robot tasks," in *2022 International Conference on Robotics and Automation (ICRA)*. IEEE, 2022, pp. 6853–6859.

[4] J. Alonso-Mora, S. Baker, and D. Rus, "Multi-robot formation control and object transport in dynamic environments via constrained optimization," *The International Journal of Robotics Research*, vol. 36, no. 9, pp. 1000–1021, 2017.

[5] P. Culbertson, J.-J. Slotine, and M. Schwager, "Decentralized adaptive control for collaborative manipulation of rigid bodies," *IEEE Transactions on Robotics*, vol. 37, no. 6, pp. 1906–1920, 2021.

[6] W. Liu, J. Hu, H. Zhang, M. Y. Wang, and Z. Xiong, "A novel graph-based motion planner of multi-mobile robot systems with formation and obstacle constraints," *IEEE Transactions on Robotics*, vol. 40, pp. 714–728, 2023.

[7] G. A. Kaminka, R. Schechter-Glick, and V. Sadov, "Using sensor morphology for multirobot formations," *IEEE Transactions on Robotics*, vol. 24, no. 2, pp. 271–282, 2008.

[8] K.-K. Oh, M.-C. Park, and H.-S. Ahn, "A survey of multi-agent formation control," *Automatica*, vol. 53, pp. 424–440, 2015.

[9] J. Hu, P. Bhowmick, I. Jang, F. Arvin, and A. Lanzon, "A decentralized cluster formation containment framework for multirobot systems," *IEEE Transactions on Robotics*, vol. 37, no. 6, pp. 1936–1955, 2021.

[10] W. Guanghua, L. Deyi, G. Wenyan, and J. Peng, "Study on formation control of multi-robot systems," in *2013 Third international conference on intelligent system design and engineering applications*. IEEE, 2013, pp. 1335–1339.

[11] J. P. Desai, J. Ostrowski, and V. Kumar, "Controlling formations of multiple mobile robots," in *Proceedings. 1998 IEEE International Conference on Robotics and Automation (Cat. No. 98CH36146)*, vol. 4. IEEE, 1998, pp. 2864–2869.

[12] G. Antonelli, F. Arrichiello, F. Caccavale, and A. Marino, "Decentralized time-varying formation control for multi-robot systems," *The International Journal of Robotics Research*, vol. 33, no. 7, pp. 1029–1043, 2014.

[13] S. He, M. Wang, S.-L. Dai, and F. Luo, "Leader–follower formation control of usvs with prescribed performance and collision avoidance," *IEEE transactions on industrial informatics*, vol. 15, no. 1, pp. 572–581, 2018.

[14] G. A. Di Caro and A. W. Z. Yousaf, "Multi-robot informative path planning using a leader-follower architecture," in *2021 IEEE International Conference on Robotics and Automation (ICRA)*. IEEE, 2021, pp. 10 045–10 051.

[15] M. A. Lewis and K.-H. Tan, "High precision formation control of mobile robots using virtual structures," *Autonomous robots*, vol. 4, no. 4, pp. 387–403, 1997.

[16] D. Roy, A. Chowdhury, M. Maitra, and S. Bhattacharya, "Multi-robot virtual structure switching and formation changing strategy in an unknown occluded environment," in *2018 IEEE/RSJ International Conference on Intelligent Robots and Systems (IROS)*. IEEE, 2018, pp. 4854–4861.

[17] S. K. Tse, Y. B. Wong, J. Tang, P. Duan, S. W. W. Leung, and L. Shi, "Relative state formation-based warehouse multi-robot collaborative parcel moving," in *2021 4th IEEE International Conference on Industrial Cyber-Physical Systems (ICPS)*. IEEE, 2021, pp. 375–380.

[18] N. E. Leonard and E. Fiorelli, "Virtual leaders, artificial potentials and coordinated control of groups," in *Proceedings of the 40th IEEE conference on decision and control (Cat. No. 01CH37228)*, vol. 3. IEEE, 2001, pp. 2968–2973.

[19] M. Egerstedt and X. Hu, "Formation constrained multi-agent control," *IEEE transactions on robotics and automation*, vol. 17, no. 6, pp. 947–951, 2001.

[20] Q. Li, F. Gama, A. Ribeiro, and A. Prorok, "Graph neural networks for decentralized multi-robot path planning," in *2020 IEEE/RSJ international conference on intelligent robots and systems (IROS)*. IEEE, 2020, pp. 11 785–11 792.

[21] Q. Li, W. Lin, Z. Liu, and A. Prorok, "Message-aware graph attention networks for large-scale multi-robot path planning," *IEEE Robotics and Automation Letters*, vol. 6, no. 3, pp. 5533–5540, 2021.

[22] J. Blumenkamp, S. Morad, J. Gielis, and A. Prorok, "Covis-net: A cooperative visual spatial foundation model for multi-robot applications," in *8th Annual Conference on Robot Learning*.

[23] M. Oquab, T. Darcet, T. Moutakanni, H. Vo, M. Szafraniec, V. Khalidov, P. Fernandez, D. Haziza, F. Massa, A. El-Nouby *et al.*, "Dinov2: Learning robust visual features without supervision," *arXiv preprint arXiv:2304.07193*, 2023.

[24] A. Vaswani, N. Shazeer, N. Parmar, J. Uszkoreit, L. Jones, A. N. Gomez, Ł. Kaiser, and I. Polosukhin, "Attention is all you need," *Advances in neural information processing systems*, vol. 30, 2017.

[25] A. Der Kiureghian and O. Ditlevsen, "Aleatory or epistemic? does it matter?" *Structural safety*, vol. 31, no. 2, pp. 105–112, 2009.

[26] A. Kendall and Y. Gal, "What uncertainties do we need in bayesian deep learning for computer vision?" *Advances in neural information processing systems*, vol. 30, 2017.

[27] V. Peretroukhin, M. Giamou, D. M. Rosen, W. N. Greene, N. Roy, and J. Kelly, "A smooth representation of belief over so(3) for deep rotation learning with uncertainty," in *Robotics: Science and Systems (RSS) 2020*, Corvallis, Oregon, USA, July 12–16 2020.

[28] Y. Gal and Z. Ghahramani, "Dropout as a bayesian approximation: Representing model uncertainty in deep learning," in *international conference on machine learning*. PMLR, 2016, pp. 1050–1059.

[29] S. K. Ramakrishnan, A. Gokaslan, E. Wijmans, O. Maksymets, A. Clegg, J. Turner, E. Undersander, W. Galuba, A. Westbury, A. X. Chang *et al.*, "Habitat-Matterport 3D Dataset (HM3D): 1000 large-scale 3D environments for embodied AI," in *Thirty-fifth Conference on Neural Information Processing Systems Datasets and Benchmarks Track*, 2021.

[30] C. Guo, G. Pleiss, Y. Sun, and K. Q. Weinberger, "On calibration of modern neural networks," in *International Conference on Machine Learning (ICML)*, 2017, pp. 1321–1330.

[31] E. Ilg, Ö. Çiçek, S. Galesso, A. Klein, O. Makansi, F. Hutter, and T. Brox, "Uncertainty estimates and multi-hypotheses networks for

optical flow," in *Proceedings of the European Conference on Computer Vision (ECCV)*, 2018, pp. 652–667.